Research Article Vol. 37, No. 12 / December 2020 / Journal of the Optical Society of America A 1895

Journal of the Optical Society of America A

OPTICS, IMAGE SCIENCE, AND VISION

Systematic analysis of frequency dependent differential photoacoustic cross-section data for source size estimation

ANUJ KAUSHIK, AVIJIT PAUL, AND RATAN K. SAHA*

Department of Applied Sciences, Indian Institute of Information Technology Allahabad, Jhalwa, Allahabad, 211015, India
**Corresponding author: ratank.saha@iiita.ac.in*

Received 10 September 2020; accepted 19 October 2020; posted 21 October 2020 (Doc. ID 409955); published 10 November 2020

A frequency dependent differential photoacoustic cross-section (DPACS) over a large frequency band (100–1000 MHz) was computed, and subsequently, morphological parameters of a photoacoustic (PA) source were quantified. The Green's function approach was utilized for calculating the DPACS for spheroidal droplets with varying aspect ratios, Chebyshev particles with different waviness and deformation parameters, and normal red blood cells and cells affected by hereditary disorders (e.g., spherocytosis, elliptocytosis, and stomatocytosis). The theoretical framework considers that PA waves propagate through an acoustically dispersive and absorbing medium and are detected by a planar detector of finite size. The frequency dependent DPACS profile was fitted with tri-axial ellipsoid, finite cylinder, and toroid form factor models to obtain size and shape information of the PA source. The tri-axial ellipsoid form factor model was found to provide better estimates of the shape parameters compared to other models for a variety of sources. The inverse problem framework may motivate developing PA-based technology to assess single-cell morphology.

https://doi.org/10.1364/JOSAA.409955

1. INTRODUCTION

Normal red blood cells (RBCs) are astonishingly deformable and stable, enabling them to travel through capillaries and perform regular physiological functions [1]. A healthy erythrocyte also does not have any nucleus and appears as a biconcave disc in the absence of external forces. This particular shape has a high surface-to-volume ratio (S/V), which is strongly correlated with its normal activities. Genetic disorders, contagious diseases, viral infections, and changes in blood chemistry can alter the erythrocyte shape, reducing its ability to bend and deform. Alteration in the shape of RBCs obstructs the blood circulation and generally becomes the reason for tissue necrosis [2]. Apart from the above medical conditions, there are several hereditary disorders where RBCs cannot retain the biconcave shape [3]. Hereditary spherocytosis, elliptocytosis, and stomatocytosis (see top row of Fig. 1) are such disorders [1,3,4]. One out of 2000 humans in the Caucasian race suffer from the first two disorders. In general, in these cases, the cohesion between the lipid bi-layer and cytoskeleton is weakened by the membrane proteins or integrity of cytoskeleton, resulting in the loss of surface area (decrease in S/V) and irreversible shape change [1]. Deformed RBCs are recognized as diseased cells by the spleen (a secondary immune organ of the human body) and consequently removed from circulation, which leads to serious blood-related disorders (e.g., hemolytic anemia).

Current computerized diagnostic methods use electrical impedance or light-scattering techniques to determine RBC concentration and mean corpuscular volume [5]. For example, Gienger *et al.* used an optical flow cytometry technique to capture the shape and size properties of RBCs. The effect of hydrodynamic forces that change the structure of RBCs has also been examined [6,7]. The techniques, namely, cytology, blood smear microscopic examination, and ektacytometry, have been employed to identify hemolytic anemia, by distinguishing the shape of RBCs. These techniques are arduous and time consuming. In the case of cytology, it is also very difficult to find cells with moderate spherocytosis or elliptocytosis.

The generation of acoustic waves due to absorption of light by a material containing chromophores is known as the photoacoustic (PA) effect. Generally, a short pulsed laser (operating in the visible to near-infrared region) illuminates a tissue, which absorbs light and produces wide band (kHz to GHz) pressure waves due to thermoelastic expansion. Ultrasound transducers capture such waves and convert them into electrical signals. Several groups have successfully captured the PA signals at a single-cell level. For example, Galaza *et al.* used diagnostic ultrasound transducers (≈3.5 to 20 MHz) to detect the PA signals from diseased cells (e.g., malaria infected cells, sickle cells, circulatory tumor cells, etc.) in circulation *in vivo* [8–10]. Strohm *et al.* measured PA signals using ultra-high-frequency

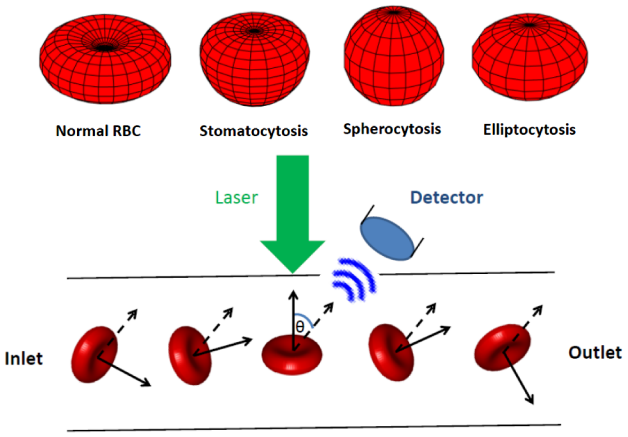

Fig. 1. Top row: surface plots (in 3D) of normal RBC and cells suffering from hereditary disorders. Bottom row: visualization of a PA flow cytometry setup. The solid arrow represents the axis of symmetry, and the dashed arrow indicates the direction of measurement.

transducers (few hundred megahertz to gigahertz) from normal and deformed RBCs [2,11,12]. PA signal analysis has also been performed to determine the nucleus-to-cytoplasmic ratio of cancer cells [13]. It is a general parameter often utilized to assess cell malignancy. They demonstrated that size and shape parameters of the light absorbing cells dictate spectral features above 100 MHz [2,11].

Therefore, a natural question is, would it be possible to obtain morphological parameters of the PA source from a measured single-particle spectrum? People believe that it may be possible, leading to development of a new instrument, namely, a PA flow cytometer for *in vitro*/*in vivo* characterization of abnormal cells in the blood stream to diagnose and combat deadly diseases. The advantage of the PA technique is that an automated system capable of measuring a large sample size in a realistic time frame can be developed. A schematic diagram of the proposed flow cytometer for *in vitro* studies is presented in Fig. 1 (bottom row). The source region contains chromophores. The ambient medium (e.g., saline water) does not have chromophores. Thus, the incident light pulse selectively heats up a certain domain producing the PA signals. This holds for optical wavelengths spanning 532–1064 nm, where most PA experiments are carried out. It is clear in the figure that the PA signals are collected from individual cells with arbitrary orientations. Moreover, a single PA radio-frequency line from a source has to be recorded within 100 ms for a typical pulsed laser with 10 Hz as the pulse repetition frequency. Therefore, for example, signals from 10 cells would be acquired in 1 s. Fluid should flow in a controlled manner so that each time laser pulse illuminates an individual cell.

We considered a quantity called the differential PA cross-section (DPACS) as a metric to study the effects of size and shape of a source on the emitted PA field [14–16]. The expression for DPACS is derived by defining it as the acoustic power received by a detector situated far away from the source divided by the intensity of the incident light beam per unit solid angle. Essentially, we applied the Green's function approach to compute the PA field generated by a particle of interest and, accordingly, DPACS was evaluated. It is analogous to the differential scattering cross-section that has been analyzed theoretically and experimentally in many fields to obtain properties of the scatterer. We examined variation of DPACS with frequency for a large set of objects such as spheroidal particles with varying aspect ratios (ARs), Chebyshev particles with different waviness (n) and deformation (ε) parameters, and normal and pathological RBCs [14]. We also investigated changes of DPACS as a function of polar angle at 390 MHz for these particles and subsequently demonstrated that the DPACS curves can be fitted with the tri-axial ellipsoid form factor (TAEFF) and cylinder form factor (CFF) models to assess their morphological parameters [15,16]. Recently, we deployed the Born series method to calculate the pressure field generated by an acoustically inhomogeneous source [17]. The numerical results emphasize that the traditional Born series method provides an accurate solution for a large source with high speed of sound contrast (−11% to 22%), but the convergent Born series technique further extends these limits.

The aim of the paper is twofold. In the forward problem, we examine how DPACS varies with frequency (100–1000 MHz) when measured by a finite detector. The coupling fluid medium between the source and the transducer is assumed to be acoustically dispersive and lossy as well. In the inverse problem, the DPACS curve averaged over many orientations generated by a test object as mentioned above is fitted with the form factor models to extract shape parameters. Besides the TEAFF and CFF models, we also employ the toroid form factor (TFF) model in this work for this purpose. To the best of our knowledge, this is the first time it has been shown, using numerical simulation, that the morphological parameters of a PA source can be extracted from the DPACS spectrum. The detailed derivations of these models are presented in this work. The performance of the models is investigated rigorously for different biological targets. The TAEFF model provides accurate estimates for particles resembling ellipsoids. The TFF and CFF models seem to be inferior compared to the TEAFF model in assessing the shape parameters of cells. The theoretical framework developed here may find application to analyze experimental data for assessing cellular morphology.

The layout of the paper is as follows. The forward and inverse problem frameworks are discussed in Section 2. Realistic signal simulation, spectrum analysis protocols, and numerical methods implemented in this study are described in Section 3. The simulation results are highlighted in Section 4. Some of the important aspects of this study are presented in Section 5, and the conclusions of this study are drawn in this section as well.

2. THEORETICAL FRAMEWORK

A. Forward Framework

The PA wave equation in the frequency domain after satisfying thermal and stress confinements can be expressed as [18]

$$\nabla^2 p + k^2 p = \begin{cases} \frac{i\omega\mu\beta I_0}{C_P}, & \text{within the source} \\ 0, & \text{in the surrounding medium,} \end{cases} \quad (1)$$

where μ, β, and C_P are the optical absorption coefficient, isobaric thermal expansion coefficient, and specific heat for the absorbing region, respectively. Here, I_0, ω, and k indicate the intensity of the light beam, modulation frequency of the light beam, and wave number of the acoustic wave, respectively. Equation (1) assumes that the source is acoustically homogeneous with respect to the surrounding medium (acoustic impedance mismatch is small) and light distribution inside it is uniform. Moreover, the media inside and outside the source are acoustically nondispersive and nonabsorbing. The solution to Eq. (1) using the Green's function approach becomes [14,15]

$$p_{\text{ext}}(\mathbf{r}, k) = \int_{V_{\text{vol}}} \frac{i\mu\beta I_0\omega}{C_P} G(\mathbf{r}|\mathbf{r}_0)\mathrm{d}^3\mathbf{r}_0, \tag{2}$$

where $G(\mathbf{r}|\mathbf{r_0}) = -\frac{e^{ik|\mathbf{r}-\mathbf{r_0}|}}{4\pi|\mathbf{r}-\mathbf{r_0}|}$ is the free-space Green's function, with $\mathbf{r}(r, \theta, \phi)$ and $\mathbf{r}_0(r_0, \theta_0, \phi_0)$ as the field and source points, respectively [19]; V_{vol} represents the volume of the PA source. A representative PA geometry in two dimensions is shown in Fig. 2 (top row). The subscript ext indicates that the field point is situated outside the PA source (i.e., $r > r_0$). Equation (2) for a homogeneous source and in the far-field approximation ($r >> r_0$) can be written as

$$\begin{aligned} p_{\text{ext}}(\mathbf{r}, k) &\approx -\frac{e^{ikr}}{4\pi r}\frac{i\mu\beta I_0\omega}{C_P}\int_{V_{\text{vol}}} e^{-i\mathbf{k}\cdot\mathbf{r_0}} d^3\mathbf{r}_0 \\ &= -\frac{e^{ikr}}{4\pi r}\frac{i\mu\beta I_0\omega}{C_P}\Upsilon \\ &= \frac{e^{ikr}}{r}M(\mathbf{k}), \end{aligned} \tag{3}$$

where

$$\Upsilon = \int_{V_{vol}} e^{-i\mathbf{k}\cdot\mathbf{r_0}}\mathrm{d}^3\mathbf{r}_0, \tag{4}$$

and $M(\mathbf{k}) = -i\mu\beta I_0\omega\Upsilon/(4\pi C_P)$ is the amplitude of the outgoing spherical wave generated by the PA source, and hence, DPACS can be defined as [14,15]

$$\sigma(k, \theta) = \frac{|M(\mathbf{k})|^2}{2\rho v I_0}, \tag{5}$$

where ρ and v are the density and speed of sound of the surrounding medium, respectively. It has been proposed by us by drawing an analogy with a differential scattering cross-section, which has been computed and measured in numerous fields to study scattering properties of inhomogeneity.

B. Inverse Framework

The integration in Eq. (4) *vis-à-vis* Eq. (5) can be calculated analytically for regular objects providing closed-form formulas for $\sigma(\mathbf{k})$. For example, Eq. (5) for a spheroidal particle becomes [20,21]

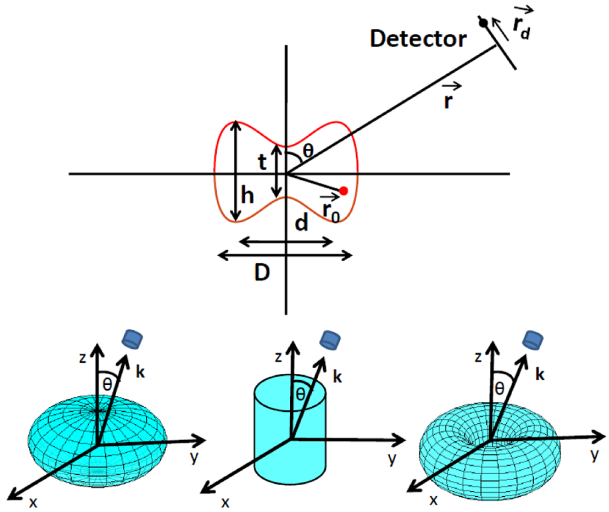

Fig. 2. Top row: geometry of the PA setup. Bottom row: surface plots of the model particles used in form factor calculations (left to right: tri-axial ellipsoid, cylinder, and toroid).

$$\begin{aligned} \Upsilon &= \int_{V_{\text{vol}}} e^{-i(k_x x_0 + k_y y_0 + k_z z_0)}\mathrm{d}x_0\mathrm{d}y_0\mathrm{d}z_0 \\ &= \frac{\rho_2\rho_3}{\rho_1^2}\int_{V_{\text{vol}}} e^{-i(k'_x x'_0 + k'_y y'_0 + k'_z z'_0)}\mathrm{d}x'_0\mathrm{d}y'_0\mathrm{d}z'_0 \\ &= \frac{4\pi\rho_1\rho_2\rho_3}{3}\frac{3j_1(k'\rho_1)}{k'\rho_1}, \end{aligned} \tag{6}$$

assuming $k'_x = k_x$, $k'_y = k_y\rho_2/\rho_1$, $k'_z = k_z\rho_3/\rho_1$, $x'_0 = x_0$, $y'_0 = \rho_1 y_0/\rho_2$, $z'_0 = \rho_1 z_0/\rho_3$, where ρ_1, ρ_2, and ρ_3 are the semi-axes of the spheroidal particle, and $k' = \frac{k}{\rho_1}\sqrt{\rho_1^2\sin^2\theta\cos^2\phi + \rho_2^2\sin^2\theta\sin^2\phi + \rho_3^2\cos^2\theta}$; j_1 is the spherical Bessel function of order unity. Thus, Eq. (6) leads to

$$\sigma(k, \theta) = \frac{\mu^2\beta^2 I_0\omega^2}{2\rho v C_P^2}\frac{V_{vol}^2}{16\pi^2}FF^2, \tag{7}$$

where

$$FF = 3j_1(k'\rho_1)/(k'\rho_1)$$

is known as the TAEFF. Figure 2 (bottom row, left panel) displays the geometrical configuration of a spheroidal particle. We mention here that size and shape information of the PA source are retained in *FF*. Moreover, $FF \to 1$ for a small particle. The form factor models have been extensively used in the literature to evaluate the size of scattering objects [20].

Similarly, for a uniform cylinder of radius Γ and length L (Fig. 2, bottom row, middle panel), Υ can be derived as [21]

$$\begin{aligned} \Upsilon &= \int_0^{\Gamma}\int_0^{2\pi}\int_{-\frac{L}{2}}^{\frac{L}{2}} e^{-i(kz_0\cos\theta + kr_0\sin\theta\cos\psi_0)} r_0\mathrm{d}r_0\mathrm{d}\psi_0\mathrm{d}z_0 \\ &= \pi\Gamma^2 L\frac{2J_1(k\Gamma\sin\theta)}{k\Gamma\sin\theta}\frac{\sin(k\frac{L}{2}\cos\theta)}{k\frac{L}{2}\cos\theta}, \end{aligned} \tag{8}$$

where J_1 is the Bessel function of order one. Therefore, the expression for the CFF can be cast as

$$FF = \frac{2J_1(k\Gamma \sin(\theta))}{k\Gamma \sin(\theta)} \frac{\sin(k\frac{L}{2}\cos(\theta))}{k\frac{L}{2}\cos(\theta)}. \tag{9}$$

Equation (4) for a toroid, whose plane is perpendicular to the z axis as shown in Fig. 2 (bottom row, right panel), can be calculated as [22]

$$\begin{aligned}\Upsilon &= \int_{-R_c}^{+R_c}\int_0^{2\pi}\int_{R_-}^{R_+} e^{-i[kz_0\cos\theta + kr_0\sin\theta\cos\psi_0]} r_0 \mathrm{d}r_0 \mathrm{d}\psi_0 \mathrm{d}z_0 \\ &= 2\pi \int_{-R_c}^{+R_c} [R_+ J_1(kR_+\sin\theta) - R_- J_1(kR_-\sin\theta)] \\ &\quad \times \frac{\cos(kz_0\cos\theta)}{k\sin\theta}\mathrm{d}z_0. \end{aligned} \tag{10}$$

Here, $R_+ = R_t + \sqrt{R_c^2 - z_0^2}$, and $R_- = R_t - \sqrt{R_c^2 - z_0^2}$; R_t and R_c are the toroid radius and cross-sectional radius, respectively. Therefore, the TFF can be expressed as [22]

$$\begin{aligned}FF &= \frac{1}{\pi R_c^2 R_t}\int_{-R_c}^{+R_c} [R_+ J_1(kR_+\sin\theta) - R_- J_1(kR_-\sin\theta)]] \\ &\quad \times \frac{\cos(kz_0\cos\theta)}{k\sin\theta}\mathrm{d}z_0. \end{aligned} \tag{11}$$

In this work, numerically generated frequency dependent DPACS curves for various particles analogous to biological targets are fitted with the TAEFF, CFF, and TFF models to extract morphological parameters.

C. PA Sources Considered in This Study

The rotation of an ellipse around its major/minor axis produces a prolate/oblate spheroid. The distance of a point that lies on the surface of a spheroid is given by

$$r'(\theta') = \frac{ab}{[b^2\sin^2\theta' + a^2\cos^2\theta']^{1/2}}, \tag{12}$$

with a and b the semi-axes, respectively, for prolate spheroid $b > a$ and for oblate spheroid $b < a$.

The Chebyshev shape can be produced as [23]

$$r'(\theta') = R_{cb}[1 + \epsilon\cos n\theta'], \tag{13}$$

where n and ϵ are the waviness and deformation parameters, respectively; R_{cb} is the radius of the unperturbed sphere. Chebyshev particles have found wide applications in many streams of science and engineering to model shapes of particles of interest. These particles are nonspherical and symmetric about the z axis.

In this work, we employ the Yurkin model to generate the contour of normal RBCs in 3D (left image of top row in Fig. 1). It is given by [24–26]

$$\xi^4 + 2R_4\xi^2 z^2 + z^4 + R_1\xi^2 + R_2 z^2 + R_3 = 0. \tag{14}$$

It has four degrees of freedom. The numerical values of R_1, R_2, R_3, and R_4 can be determined from the morphological parameters of RBCs [e.g., diameter (D), dimple thickness (t), maximum height (h), and diameter of the circle passing through the maximum height (d)]. The morphological parameters are shown in Fig. 2 (top row).

3. NUMERICAL METHOD

A. Computation of Realistic PA Signal and Spectrum Analysis

Consider that the PA waves generated by a source propagate through a lossy and dispersive medium. Therefore, the PA field detected by a point detector can be cast as [27,28]

$$\begin{aligned}p_{\mathrm{ext}}(\mathbf{r},\omega) = -\int_{V_{\mathrm{vol}}} \frac{i\mu\beta I_0\omega}{C_P}\frac{e^{i\omega|\mathbf{r}-\mathbf{r}_0|/v}}{4\pi|\mathbf{r}-\mathbf{r}_0|} \\ \times e^{-\alpha_0|\mathbf{r}-\mathbf{r}_0|[|\omega|^\gamma - i\tan(\pi\gamma/2)\omega|\omega|^{\gamma-1}]} d^3\mathbf{r}_0. \end{aligned} \tag{15}$$

Here, it is assumed that the acoustic attenuation coefficient (α) follows a frequency power law such as [27]

$$\alpha = \alpha_0\omega^\gamma, \tag{16}$$

where α_0 and γ are the prefactor and exponent of the power law, respectively. The numerical value of γ typically lies between one and two for soft tissue [27]. Note that the second exponential in Eq. (15) has two parts. The first and second parts arise because of attenuation and dispersion of the acoustic waves, respectively. These two factors together satisfy the causality condition and are also connected through the Kramers–Kronig relations [27].

For a finite detector, the average field can be obtained as

$$\begin{aligned}p_{\mathrm{ext}}^{\mathrm{avg}}(\mathbf{r},\omega) = \frac{-1}{A_d}\int_{A_d} d^2\mathbf{r}_d \int_{V_{\mathrm{vol}}} \frac{i\mu\beta I_0\omega}{C_P}\frac{e^{i\omega|\mathbf{r}+\mathbf{r}_d-\mathbf{r}_0|/v}}{4\pi|\mathbf{r}+\mathbf{r}_d-\mathbf{r}_0|} \\ \times e^{-\alpha_0|\mathbf{r}+\mathbf{r}_d-\mathbf{r}_0|[|\omega|^\gamma - i\tan(\pi\gamma/2)\omega|\omega|^{\gamma-1}]} \mathrm{d}^3\mathbf{r}_0, \end{aligned} \tag{17}$$

where $\mathbf{r}$ and $\mathbf{r}_d$ indicate the position vectors for the center of the detector and a point on the detector, respectively; A_d denotes the surface area of the detector normal to $\mathbf{r}$; the superscript avg states the average field. A schematic diagram is shown in Fig. 2 (top row). The corresponding time domain signal for a delta function heating pulse can be calculated as

$$p_{\mathrm{m}}(t) = \frac{1}{2\pi}\int_{-\infty}^{\infty} p_{\mathrm{ext}}^{\mathrm{avg}}(\mathbf{r},\omega)e^{-i\omega t}\mathrm{d}\omega, \tag{18}$$

where the subscript m stands for measured signal. Equation (18) can be evaluated to obtain time series PA pressure data (or PA signal) generated by a source and when the waves propagate through an acoustically lossy and dispersive medium. Further, artificial random noise can be added with such a simulated signal to mimic an experimental situation.

The attenuation compensated spectrum averaged over many orientations (N_o) of the source is given by

$$S_m(\omega) = \langle[|\mathfrak{F}(p_{\mathrm{m}})|e^{\alpha_0\omega^\gamma r}]^2\rangle, \tag{19}$$

where $\mathfrak{F}$ is the Fourier transform operator, and $< >$ denotes the ensemble average (i.e., over many orientations). Therefore, the DPACS becomes

$$\sigma_O(\omega) = \frac{S_m r^2}{2\rho v I_0}. \tag{20}$$

The subscript O indicates that σ is averaged over many orientations.

Size and shape parameters of a PA source can be extracted using various form factor models if σ_o is known. Two approaches are employed herein to accomplish this. In the first method (referred to as method 1 in the text), we iteratively minimize the following quantity as

$$\Omega = \sum_i \frac{\left| \frac{\sigma_{\mathrm{OT}}(\omega_i)}{\sigma_{\mathrm{OR}}(\omega_i)} - \frac{V_{\mathrm{T}}^2 FF_{\mathrm{OT}}^2(\omega_i)}{V_{\mathrm{R}}^2 FF_{\mathrm{OR}}^2(\omega_i)} \right|}{\frac{\sigma_{\mathrm{OT}}(\omega_i)}{\sigma_{\mathrm{OR}}(\omega_i)}}, \tag{21}$$

where V_T and V_R are the volume of the test and reference particles, respectively; σ_{OT} and σ_{OR} are the orientation averaged DPACS for those particles, respectively, and FF averaged over many orientations is given by

$$FF_O = \frac{1}{2}\int_0^{\pi} FF^2 \sin\theta \mathrm{d}\theta. \tag{22}$$

The exact values of shape parameters of the reference particle are known *a priori*.

In the second approach (termed as method 2 in the text), the following quantity is minimized iteratively:

$$\Omega = \sum_i \frac{\left| \frac{\sigma_{\mathrm{OT}}(\omega_i)/\max[\sigma_{\mathrm{OT}}(\omega_i)]}{\sigma_{\mathrm{OR}}(\omega_i)/\max[\sigma_{\mathrm{OR}}(\omega_i)]} - \frac{FF_{\mathrm{OT}}^2(\omega_i)}{FF_{\mathrm{OR}}^2(\omega_i)} \right|}{\frac{\sigma_{\mathrm{OT}}(\omega_i)/\max[\sigma_{\mathrm{OT}}(\omega_i)]}{\sigma_{\mathrm{OR}}(\omega_i)/\max[\sigma_{\mathrm{OR}}(\omega_i)]}}. \tag{23}$$

In this work, both methods are deployed to assess the shape parameters of spheroidal and Chebyshev particles, whereas only method 1 is applied to RBCs.

B. Physical Parameters

The optical and thermo-mechanical parameters for the absorbing object were taken as- $I_0 = 1.51 \times 10^{12}\,\mathrm{Jm^{-2}\,s^{-1}}$, $\mu = 809.02\,\mathrm{m^{-1}}$, $\beta = 1.5 \times 10^{-4}\,\mathrm{K^{-1}}$, $C_P = 3.23 \times 10^3\,\mathrm{Jkg^{-1}\,K^{-1}}$ [15]. The density and the speed of sound of the surrounding medium were chosen as $\rho = 1005\,\mathrm{kg/m^3}$ and $v = 1498\,\mathrm{m/s}$, respectively [15]. The frequency dependent attenuation parameters were chosen as $\alpha_0 = 5.5 \times 10^{-10}\,\mathrm{Np(rad/s)^{-\gamma}\,m^{-1}}$, $\gamma = 1.5$ [27]. These numerical values correspond to those of common body fluids or tissues. The average spectrum was computed over $N_O = 200$ orientations. Table 1 displays the numerical values of the parameters considered in this study.

C. Shape Parameters

In this work, we studied spheroidal particles with AR = 1:8, 1:4, 1:2, 2:1, 4:1, and 8:1, Chebyshev particles with different waviness parameters $n = 2$, 4, 6, and deformation parameters $\epsilon = \pm 0.25$. Four higher-order Chebyshev particles were also considered with $n = 35$, 45, and deformation parameters $\epsilon = \pm 0.05$ [29]. The volume was taken as constant ($523.6\,\mu\mathrm{m^3}$) for all spheroidal and Chebyshev particles. These numerical values are presented in Table 2.

Surface plots of normal and pathological RBCs are displayed in Fig. 1 (top row). The Yurkin model was employed to obtain the 3D shape of normal RBCs. The four morphological parameters corresponding to normal RBCs (row 5, Table 2) were utilized to find out the parameters (R_1, R_2, R_3, and R_4) of the Yurkin model. The shape mimicking stomatocyte (ST) was produced by varying these parameters phenomenologically (row 6, Table 2). The upper half for ST was generated using Eq. (14); however, the lower part was assumed to be a half-sphere. Two shapes originating from hereditary disorders, referred to as spherocyte (SC) and elliptocyte (EC), were also included in the study. The associated values of AR were taken from the literature and are given in rows 7–8, Table 2, respectively.

Table 1. Physical Parameters Taken in Computation

ρ	$1005\,\mathrm{kg/m^3}$
v	1498 m/s
μ	$809.02\,\mathrm{m^{-1}}$
β	$1.5 \times 10^{-4}\,\mathrm{K^{-1}}$
C_P	$3.23 \times 10^3\,\mathrm{Jkg^{-1}\,K^{-1}}$
I_0	$1.51 \times 10^{12}\,\mathrm{Jm^{-2}\,s^{-1}}$
α_0	$5.5 \times 10^{-10}\,\mathrm{Np\,(rad/s)^{-\gamma}\,m^{-1}}$
γ	1.5
r	100 μm
A_d	$5.03 \times 10^3\,\mu\mathrm{m^2}$
N_O	200

Table 2. Shape Parameters Utilized in Calculation[a]

Objects	Volume	Shape Parameters
Spheroids	523.6	b:a = 1:2, 1:4, 1:8, 2:1, 4:1, 8:1
Chebyshev	523.6	$\epsilon = \pm 0.25$, $n = 2$, 4 and 6
	523.6	$\epsilon = \pm 0.05$, $n = 35$ and 45
RBC	122.4	$D = 7.65$, $t/2 = 0.70$, $h/2 = 1.42$, $d = 0.7D$
ST	112.2	$D = 6.37$, $t/2 = 1.36$, $h/2 = 1.47$, $d = 0.7D$
SC	104.3	b:a = 1:1
EC	104.6	b:a = 7:11

[a]Unit for length parameters is in μm, and volume is in $\mu\mathrm{m^3}$.

D. Numerical Computation

Equation (17) was calculated in this work for different particles. The PA field for each particle with a random orientation was calculated over a large acoustic frequency band (100–1000 MHz, with an increment of ≈5 MHz). A planar detector with circular aperture of radius 40 μm was placed at a distance 100 μm from the center of the source to capture impinging pressure waves [11–13]. The schematic diagram is shown in Fig. 2 (top row). The volume integral in Eq. (17) was evaluated using Simpson's 1/3 rule (with grid size, $dx = dy = dz = 200$ nm) to find the PA pressure at a particular point lying on the detector. The surface integral was carried out employing the Monte Carlo method [30]. Essentially, PA fields at 500 random points lying

on the detector were calculated and then summed up to obtain average pressure recorded by the detector. This procedure was repeated for 200 random orientations of the source particle. Moreover, dimensions of the source were also varied a little bit (±2% with respect to mean length in each dimension) to introduce intra-variability among each type of source while computing PA spectra from 200 random orientations. In other words, we considered 200 slightly different particles for 200 orientations. Average spectrum (attenuation compensated) was determined from 200 different spectra [see Eq. (19)]. A computer code in C was written for this purpose and was executed in a virtual machine [CentOS, Intel Core Processor (Broadwell, IBRS)] working at 2.19 GHz, 256 GB RAM, 80 cores). It took about 10 min to run and to generate spectral data for each spheroidal particle for one orientation. After that, DPACS for the test particle was computed using Eq. (20). Similarly, DPACS for the reference particle was also obtained. The first spheroidal particle with AR = 1:2 acted as the reference particle ($a = 6.28$ μm, $b = 3.14$ μm). Note that the time domain signal was not calculated in this work (discussed below).

The next step was to vary the fitting parameters (e.g., ρ_1, ρ_2, ρ_3 for the TAEFF model; Γ and L for the CFF model; R_t and R_c for the TFF model) iteratively, and at each step, fitting error (Ω) was computed [from Eqs. (21) and (23) in the two methods, respectively] and recorded. The angular domain of θ from zero to π was uniformly divided into 200 points, and accordingly, FF_O was calculated by evaluating Eq. (22). The set of parameters with minimum Ω provided characteristic dimensions of the PA source along different directions. The spectrum analysis was performed in MATLAB.

4. NUMERICAL RESULTS

Representative plots of frequency dependent DPACS (at $\theta = \pi/4$) under various conditions for spheroids with AR = 1:4 ($a = 7.93$ μm, $b = 1.98$ μm) and 4:1 ($a = 3.14$ μm, $b = 12.56$ μm) are shown in Figs. 3(a) and 3(b), respectively, over a frequency band of 100–1000 MHz. The solid (blue) line presents the simulated PA spectrum when the pressure waves propagate through an acoustically nondispersive, lossless medium and are detected by a point detector. The dashed (red) line exhibits the calculated PA spectrum when the surrounding fluid is acoustically nondispersive and lossless and the PA waves are detected by a finite detector. The dotted (green) line shows the attenuation compensated PA spectrum measured by a finite detector, and the coupling medium is acoustically dispersive and lossy. The same plots for the Chebyshev particles with $R_{cb} = 4.93$ μm, $n = 4$, $\epsilon = 0.25$ and $R_{cb} = 4.78$ μm, $n = 4$, $\epsilon = -0.25$ are displayed in Figs. 3(c) and 3(d), respectively. These curves illustrate the well-known peaks and dips pattern. The curves (solid and dashed lines) demonstrate a good match in the low frequency range [up to nearly 420 MHz in Fig. 3(a)]. However, the curve for the finite detector slightly deviates with respect to that of the point detector in the high frequency range (>420 MHz). This may be due to the averaging effect for a detector with finite size. The oscillations in the PA spectrum for the third case (finite detector and dispersive, lossy medium) become less prominent (compared to the other two curves) approximately beyond 450 MHz. Obviously, this is due

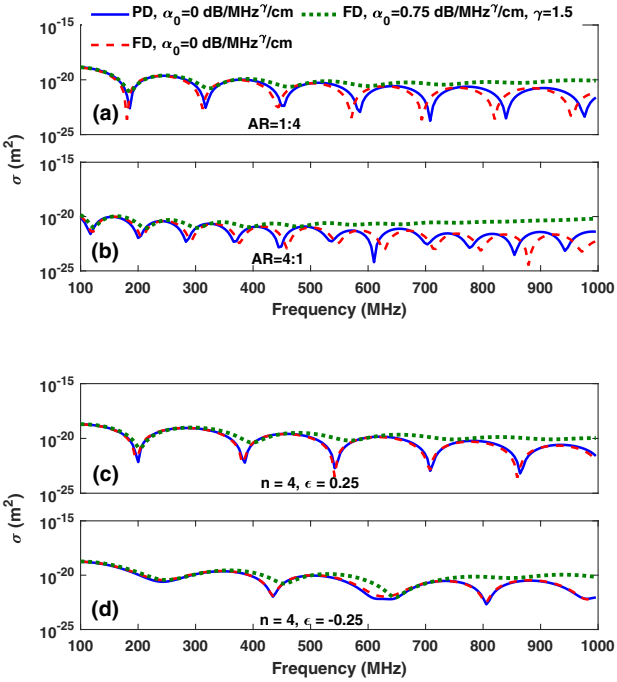

Fig. 3. (a) Plot of frequency dependent DPACS calculated at $\theta = \pi/4$ for a spheroidal particle with aspect ratio AR = 1:4. Solid line: simulated DPACS when waves are detected by a point detector (PD) and propagate through an acoustically nondispersive, lossless medium; dashed line: simulated DPACS when a finite detector (FD) is used to sense the PA waves and the medium is acoustically lossless and nondispersive; dotted line: attenuation compensated DPACS for a FD and acoustically dispersive, lossy medium. (b) Same as (a) but for a spheroidal particle with AR = 4:1. (c), (d) Similar graphs for Chebyshev particles with $n = 4$, $\epsilon = 0.25$ and $n = 4$, $\epsilon = -0.25$, respectively.

to the effects of the finite aperture of the detector and attenuation compensation. Similar trends can be observed in other figures. The number of oscillations is more in Fig. 3(b) than that of the other graphs. Further, depths of a few dips in Fig. 3(d) are less in comparison to those of the other figures. Representative plots of the DPACS as a function of frequency are shown in Fig. 4 for RBCs. The curves appear almost similar.

Plots of attenuation compensated normalized DPACS (i.e., with respect to the DPACS of the reference particle) are shown in Fig. 5 for spheroidal droplets and Chebshev particles. Best fitted curves produced by the TAEFF model for method 1 [Eq. (21)] and method 2 [Eq. (23)] are presented in the same figure as well. The TAEFF model provides in general very good fits to the simulated DPACS data over the entire frequency range. The locations of maxima and minima are well reproduced by the fitted curves. The peaks and dips of the fitted lines look more prominent compared to those of the simulated data (solid line). This is because of the fact that theoretical functions have been used for fitting, and they are valid for a point detector and nondispersive, lossless coupling medium. The numerical values of the best fit parameters are given in Table 3. The corresponding nominal values (mean ± std) are also included in the same table. It shows that the assessed morphological parameters demonstrate a good match with the actual values. In general,

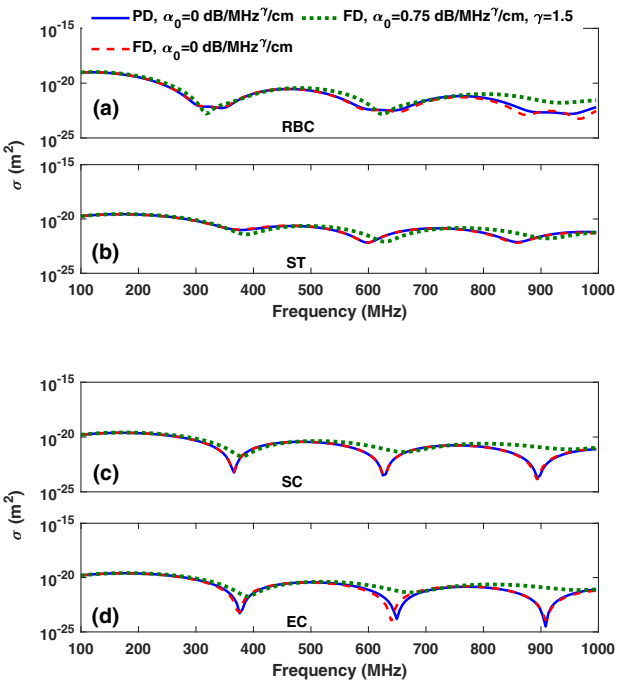

Fig. 4. (a) Variation of DPACS computed at $\theta = \pi/4$ as a function of frequency for normal RBC. Solid line: computed DPACS for a point detector (PD) and acoustically nondispersive, lossless medium; dashed line: simulated DPACS for a finite detector (FD) and acoustically nondispersive, lossless medium; dotted line: attenuation compensated DPACS for a FD and acoustically dispersive and lossy medium. (b)–(d) Same as (a) but for stomatocyte (ST), spherocyte (SC), and elliptocyte (EC), respectively.

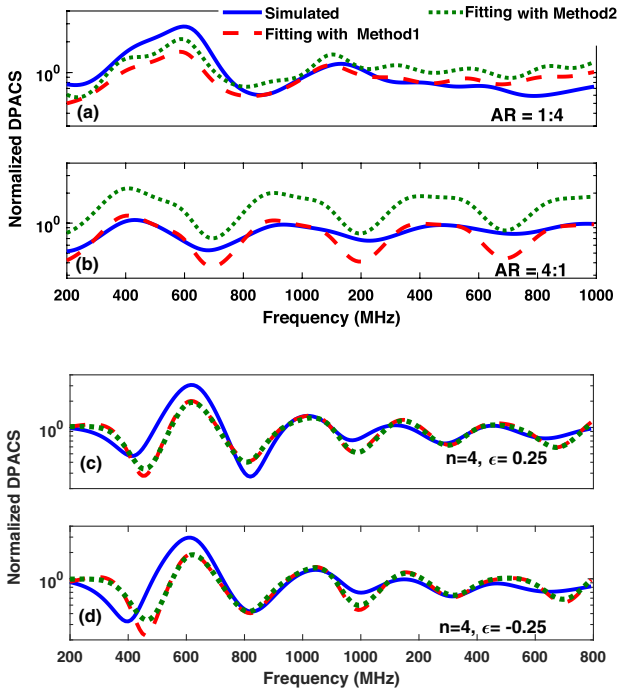

Fig. 5. (a), (b) Fitting of the frequency dependent normalized DPACS curves using the TAEFF model for spheroidal particles with aspect ratio AR = 1:4 and AR = 4:1, respectively. (c), (d) Same plots for Chebyshev particles with $n = 4$, $\epsilon = 0.25$ and $n = 4$, $\epsilon = -0.25$, respectively. Solid (blue) line plots σ_{OT}/σ_{OR} as a function of frequency; dashed (red) and dotted (green) lines are the same plots of $V_T^2 FF_{OT}^2 / V_R^2 FF_{OR}^2$ for the best fit parameters provided by method 1 and FF_{OT}^2/FF_{OR}^2 for the best fit parameters facilitated by method 2, respectively.

method 2 works better than method 1 in predicting shape and size parameters of the source particles. It is important to note that both methods perform even better for complex Chebyshev particles.

Figure 6 displays plots of the normalized DPACS (attenuation compensated) for normal and deformed RBCs. Best fitted curves for the TEAFF, CFF, and TFF models provided by method 1 are also drawn in each figure. The corresponding numerical values are included in Table 4. The TEAFF model appears to provide good fits to the simulated curves (solid lines). The fitted lines for the CFF model seems to work better for the deformed RBCs [Figs. 6(b)–6(d)] than the normal RBC. The best fitted lines for the TFF model deviate greatly for all cases, particularly in the low frequency range. Though the fittings by the form factor models seem good in some cases, estimated parameters differ significantly from the desired values. As expected, volume error for the TEAFF model is less for the SC and EC cells, but it overestimates the volume of normal RBCs (second column, Table 4). For ST, extracted shape parameters though are not accurate but exhibit valid changes (i.e., diameter shrinks and length along the symmetry axis increases). The best fit parameters of the CFF model are given in the third column of Table 4. It underestimates at least one of the shape parameters. The TFF model correctly predicts the distance of the outer periphery from the center (i.e., $R_t + R_c$) with high accuracy for normal RBCs. Note that in all cases, the ring torus ($R_c < R_t$) provided the best fits, and the predicted values are not useful. The outcomes of method 2 were not satisfactory, and that is why they are not incorporated herein.

5. DISCUSSION AND CONCLUSIONS

The time independent Helmholtz wave equation for the PA wave propagation is solved numerically using the Green's function approach for calculating fields generated by spheroidal droplets, Chebyshev particles, and normal and diseased RBCs. The coupling medium between the source and the detector was chosen to be acoustically dispersive and lossy. The detector was considered to be a finite detector. These two aspects were incorporated in this study to mimic a real situation. The frequency dependent DPACS has also been computed for each particle. The number of oscillations in the DPACS curve increases, and its first minimum appears earlier as the length of the PA source increases along the direction of measurement. The magnitude of the DPACS grows as the area perpendicular to the direction of measurement increases.

Average frequency dependent DPACS (attenuation compensated) was computed for each particle over 200 orientations, resembling an experimental situation. While computing 200 spectra, slightly different particles were considered, as discussed above. This approach essentially introduces intra-variability of each target object and contributes to uncertainty in the

Table 3. Estimated Values (Corresponding to the Best Fitted Curves) of the Morphological Parameters for Spheroidal and Chebyshev Particles Considered in This Study[a]

Nominal Values (μm)	Estimated Values (μm) Using Method 1	Estimated Values (μm) Using Method 2
$a = 6.28 \pm 0.07,\ b = 3.14 \pm 0.03,$ AR = 1:2	$\rho_1 = 6.18, \rho_3 = 3.29,$ VE = 0.60%	$\rho_1 = 6.18, \rho_3 = 3.29,$ VE = 0.60%
$a = 7.94 \pm 0.08,\ b = 1.98 \pm 0.02,$ AR = 1:4	$\rho_1 = 6.20, \rho_3 = 2.15,$ VE = 33.80%	$\rho_1 = 8.25, \rho_3 = 2.10,$ VE = 14.47%
$a = 10.0 \pm 0.10,\ b = 1.25 \pm 0.01,$ AR = 1:8	$\rho_1 = 5.80, \rho_3 = 1.40,$ VE = 62.28%	$\rho_1 = 10.5, \rho_3 = 1.40,$ VE = 23.61%
$a = 3.96 \pm 0.04,\ b = 7.94 \pm 0.08,$ AR = 2:1	$\rho_1 = 3.80, \rho_3 = 6.40,$ VE = 25.98%	$\rho_1 = 3.80, \rho_3 = 9.05,$ VE = 4.66%
$a = 3.14 \pm 0.03,\ b = 12.57 \pm 0.13,$ AR = 4:1	$\rho_1 = 3.00, \rho_3 = 8.20,$ VE = 40.89%	$\rho_1 = 3.00, \rho_3 = 11.9,$ VE = 14.22%
$a = 2.50 \pm 0.03,\ b = 20.02 \pm 0.21,$ AR = 8:1	$\rho_1 = 2.35, \rho_3 = 13.40,$ VE = 40.73%	$\rho_1 = 2.35, \rho_3 = 16.40,$ VE = 27.46%
$R_{cb} = 5.31 \pm 0.06,\ n = 2, \epsilon = 0.25$	$\rho_1 = 3.90, \rho_3 = 6.50,$ VE = 20.81%	$\rho_1 = 3.85, \rho_3 = 8.60,$ VE = 2.09%
$R_{cb} = 4.93 \pm 0.05,$ n = 4, $\epsilon = 0.25$	$\rho_1 = 4.30, \rho_3 = 6.35,$ VE = 5.96%	$\rho_1 = 4.30, \rho_3 = 7.10,$ VE = 5.14%
$R_{cb} = 4.89 \pm 0.05,$ n = 6, $\epsilon = 0.25$	$\rho_1 = 5.05, \rho_3 = 4.25,$ VE = 1.19%	$\rho_1 = 4.60, \rho_3 = 6.75,$ VE = 14.39%
$R_{cb} = 5.00 \pm 0.05,$ n = 35, $\epsilon = 0.05$	$\rho_1 = 5.00, \rho_3 = 4.40,$ VE = 11.90%	$\rho_1 = 4.70, \rho_3 = 5.35,$ VE = 5.34%
$R_{cb} = 5.00 \pm 0.05,\ n = 45, \epsilon = 0.05$	$\rho_1 = 5.00, \rho_3 = 4.40,$ VE = 11.90%	$\rho_1 = 4.70, \rho_3 = 5.35,$ VE = 5.34%
$R_{cb} = 4.53 \pm 0.05,$ n = 2, $\epsilon = -0.25$	$\rho_1 = 5.50, \rho_3 = 3.50,$ VE = 15.20%	$\rho_1 = 6.20, \rho_3 = 3.50,$ VE = 7.75%
$R_{cb} = 4.78 \pm 0.05,$ n = 4, $\epsilon = -0.25$	$\rho_1 = 4.25, \rho_3 = 6.00,$ VE = 13.20%	$\rho_1 = 4.25, \rho_3 = 7.40,$ VE = 7.04%
$R_{cb} = 4.82 \pm 0.05,\ n = 6, \epsilon = -0.25$	$\rho_1 = 5.20, \rho_3 = 4.30,$ VE = 6.87%	$\rho_1 = 5.60, \rho_3 = 4.50,$ VE = 13.02%
$R_{cb} = 5.00 \pm 0.05,$ n = 35, $\epsilon = -0.05$	$\rho_1 = 5.00, \rho_3 = 4.40,$ VE = 11.90%	$\rho_1 = 4.70, \rho_3 = 5.35,$ VE = 5.34%
$R_{cb} = 5.00 \pm 0.05,$ n = 45, $\epsilon = -0.05$	$\rho_1 = 5.00, \rho_3 = 4.40,$ VE = 11.90%	$\rho_1 = 4.70, \rho_3 = 5.35,$ VE = 5.34%

[a]Nominal values of the parameters are also presented here for comparison. Calculated volume error (VE) for each case is incorporated in the table. AR stands for aspect ratio, and the unit for a, b, R_{cb}, ρ_1, and ρ_3 is μm.

estimation. The finite size of the aperture of the detector averages out the incident pressure field and also acts as a source of uncertainty in the prediction. Measured time domain PA signals are corrupted with electronic noise, which affects the solution to the inverse problem as well. In this work, we did not calculate the time domain PA signal or add any synthetic electronic noise to such a signal. The time domain PA signal could be easily computed by taking the inverse Fourier transform of Eq. (17). The available functions (e.g., awgn in MATLAB, addNoise in the k-Wave toolbox [28]) distribute the noise power equally over the entire bandwidth of the signal. When we applied such a function to add noise to the simulated PA signals, we observed that noise power in the high frequency range (>500 MHz) became comparable to the signal power, leading to difficulty to solve the inverse problem. It is known that low noise amplifiers are used in practice to mitigate this issue while recording high frequency signals.

The normalized DPACS curves were fitted with the TAEFF, CFF, and TFF models. The arguments for which these models provided best fits to the simulated DPACS were considered

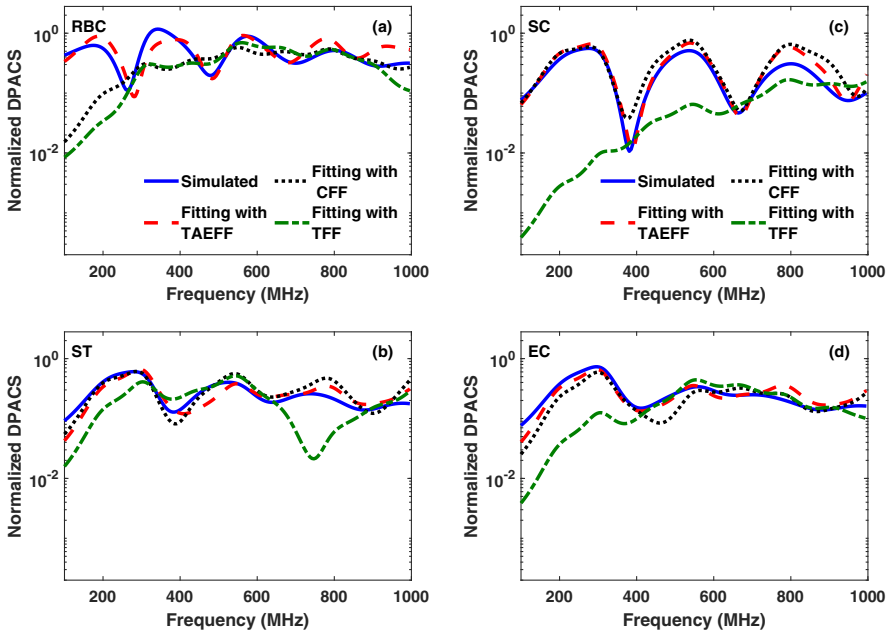

Fig. 6. (a) Normalized DPACS and fitted curves for normal RBC. (b)–(d) Same as (a) but for stomatocyte (ST), spherocyte (SC), and elliptocyte (EC), respectively. Solid (blue) line plots σ_{OT}/σ_{OR} as a function of frequency; dashed (red), dotted (black), and dashed-dotted (green) lines are the same plots of $V_T^2 FF_{OT}^2 / V_R^2 FF_{OR}^2$ for TEAFF, CFF, and TFF models, respectively, for the best fit parameters provided by method 1 for each form factor model.

Table 4. Extracted Values (for the Best Fitted Curves) of Morphological Parameters for Normal and Deformed RBCs Considered in This Study[a]

	Estimated Values (μm) Using Method 1		
Nominal Values	**TAEFF**	**CFF**	**TFF**
RBC, $D = 7.65 \pm 0.09$	$\rho_1 = 4.05, \rho_3 = 3.35$	$\Gamma = 3.45, L = 1.20$	$R_t = 2.90, R_c = 0.80$
$t/2 = 0.7, h/2 = 1.42, d = 0.7D$	VE = 88.04%	VE = 63.34%	VE = 70.06%
ST, $D = 6.37 \pm 0.07$	$\rho_1 = 2.95, \rho_3 = 1.95$	$\Gamma = 2.65, L = 3.70$	$R_t = 1.50, R_c = 1.20$
$t/2 = 1.36, h/2 = 1.47$ d $= 0.7D$	VE = 36.64%	VE = 27.24%	VE = 61.99%
SC, $a = 2.92 \pm 0.03$,	$\rho_1 = 2.65, \rho_3 = 3.00$	$\Gamma = 2.55, L = 4.50$,	$R_t = 2.20, R_c = 0.40$
$b = 2.92 \pm 0.03$, AR = 1:1	VE = 15.40%	VE = 11.86%	VE = 93.33%
EC, $a = 3.40 \pm 0.04$	$\rho_1 = 2.95, \rho_3 = 1.90$	$\Gamma = 1.95, L = 4.50$	$R_t = 1.65, R_c = 0.80$
$b = 2.16 \pm 0.02$, AR = 7:11	VE = 33.78%	VE = 48.60%	VE = 80.07%

[a]Nominal values of the parameters are presented here for comparison. Volume error (VE) is also included in the table. AR stands for aspect ratio, and the unit for D, h, t, ρ_1, ρ_3, Γ, L, R_t and R_c is μm.

as the characteristic dimensions of the source. To do so, we divided the spectrum of the test particle with that of the reference particle. Various system dependent effects were cancelled out because of this step, and thus, estimates became reliable. In this work, physical parameters of the test and reference particles were assumed to be the same and hence, allowed us to use method 1 [Eq. (21)] for size estimation. Method 2 [Eq. (23)] is more general and can be applied even when this assumption does not hold. Method 2 though worked well for the spheroidal and Chebyshev particles but did not provide reliable estimates for RBCs (data not shown). Further, investigations are required to design a robust minimization procedure with suitable constraints so that morphological information of cells can be predicted accurately.

As mentioned earlier, the underlying assumption of Eq. (1) is that light distribution inside the PA source is uniform. This assumption may not be valid in general. Fluence distribution inside the source may become inhomogeneous owing to scattering of light waves. Further, the medium inside the source was considered to be a fluid medium, which does not support shear waves. However, for RBCs, the membrane has shear and bending resistance. These properties may alter the wavevector $\mathbf{k}$ inside and outside the source. The effect of light polarization on PA emission is also required to be examined. In this work, deformation of cells due to hydrodynamic forces was ignored. Further investigations are required to address these issues. Experimental validation of the proposed methodology is needed to examine its utility in practice.

In conclusion, a theoretical model is presented for calculating frequency dependent DPACS for an arbitrary source whose impedance mismatch is small compared to the surrounding medium (resembling biological cells). The model includes the effects of dispersion, attenuation of the PA waves (while propagating through the coupling medium), and their detection with a planar detector of finite size. Simulated frequency dependent DPACS (100–1000 MHz) averaged over many orientations is generated for simple spheroidal droplets, complex Chebyshev particles, and realistic normal and deformed RBCs. The DPACS spectra are fitted with TAEFF, CFF, and TFF models to determine the morphological parameters of the PA sources. The TAEFF model, in general, provides reliable estimates for a variety of shapes. The spectrum analysis protocol needs further modification in order to employ it in practice to quantify cell shape parameters and, accordingly, differentiate normal and diseased RBCs.

Acknowledgment. The computational results reported in this work were performed at the Central Computing Facility of IIITA, Allahabad. The authors are grateful to Pankaj Warbal, Deepak Sonker, Ravi Prakash, and Amrita Mukherjee for their cooperation during this work. The anonymous reviewers are also gratefully acknowledged for thoughtful comments and suggestions, which improved the presentation and technical content of the manuscript.

Disclosures. The authors declare no conflicts of interest.

REFERENCES

1. H. Li, L. Lu, P. A. Buffet, M. Dao, G. Karniadakis, and S. Suresh, "Mechanics of diseased red blood cells in human spleen and consequences for hereditary blood disorders," Proc. Natl. Acad. Sci. USA **115**, 9574–9579 (2018).
2. E. M. Strohm, E. S. L. Berndl, and M. C. Kolios, "Probing red blood cell morphology using high-frequency photoacoustics," Biophys. J. **105**, 59–67 (2013).
3. L. D. Costa, J. Galimand, O. Fenneteau, and N. Mohandas, "Hereditary spherocytosis, elliptocytosis, and other red cell membrane disorders," Blood Rev. **27**, 167 (2013).
4. I. V. Pivkin, Z. Peng, G. E. Karniadakis, P. A. Buffet, M. Dao, and S. Suresh, "Biomechanics of red blood cells in human spleen and consequences for physiology and disease," Proc. Natl. Acad. Sci. USA **113**, 7804–7809 (2016).
5. P. Simon, M. Frankowski, N. Bock, and J. Neukammer, "Label-free whole blood cell differentiation based on multiple frequency AC impedance and light scatter analysis in a micro flow cytometer," Lab Chip **16**, 2326–2338 (2016).
6. J. Gienger, H. Gross, V. Ost, M. Bär, and J. Neukammer, "Assessment of deformation of human red blood cells in flow cytometry: measurement and simulation of bimodal forward scatter distributions," Biomed. Opt. Express **10**, 4531–4550 (2019).
7. É. Gibaud, "Numerical simulation of red blood cells flowing in a blood analyzer," Ph.D. thesis (Université Montpellier, 2015).
8. C. Cai, K. A. Carey, D. A. Nedosekin, Y. A. Menyaev, M. Sarimollaoglu, E. I. Galanzha, J. S. Stumhofer, and V. P. Zharov, "In vivo photoacoustic flow cytometry for early malaria diagnosis," Cytometry Part A **89A**, 531–542 (2016).
9. E. I. Galanzha and V. P. Zharov, "Circulating tumor cell detection and capture by photoacoustic flow cytometry in vivo and ex vivo," Cancers **5**, 1691–1731 (2013).

10. E. I. Galanzha and V. P. Zharov, "Photoacoustic flow cytometry for single sickle cell detection in vitro and in vivo," Analyt. Cellular Pathol. **2016**, 2642361 (2016).
11. E. M. Strohm, E. S. L. Berndl, and M. C. Kolios, "High frequency label free photoacoustic microscopy of single cells," Photoacoustics **1**, 49 (2013).
12. M. N. Fadhel, E. M. Strohm, and M. C. Kolios, "High frequency photoacoustic spectral analysis of erythrocyte programmed cell death (eryptosis)," in *IEEE International Ultrasonics Symposium (IUS)* (2016).
13. M. J. Moore, J. A. Sebastian, and M. C. Kolios, "Determination of cell nucleus-to-cytoplasmic ratio using imaging flow cytometry and a combined ultrasound and photoacoustic technique: a comparison study," J. Biomed. Opt. **24**, 106502 (2019).
14. R. K. Saha, S. Karmakar, A. Adhikari, and M. C. Kolios, "Photoacoustic field calculation for nonspherical axisymmetric fluid particles," Biomed. Phys. Eng. Express **3**, 015017 (2017).
15. A. Kaushik, D. Sonker, and R. K. Saha, "Study on angular distribution of differential photoacoustic cross-section and its implication in source size determination," J. Opt. Soc. Am. A **36**, 387–396 (2019).
16. A. Kaushik, D. Sonker, and R. K. Saha, "Use of angular distribution of differential photoacoustic cross-section data for estimating source size," Proc. SPIE **11077**, 110770E (2019).
17. A. Kaushik, P. K. Yallavarthy, and R. K. Saha, "Convergent Born series improves accuracy of numerical solution of time independent photoacoustic wave equation," J. Mod. Opt. **67**, 849–855 (2020).
18. G. J. Diebold, T. Sun, and M. I. Khan, "Photoacosutic monopole radiation in one, two and three dimensions," Phys. Rev. Lett. **67**, 3384–3387 (1991).
19. P. M. Morse and H. Feshbach, *Methods of Theoretical Physics* (McGraw-Hill, 1953), Chap. 7, pp. 791–895.
20. C. Alves and C. L. P. Oliveira, *Calculation of Small Angle Scattering Patterns* (IntechOpen, 2018), Chap. 1.
21. M. A. Schroer, "Small angle x-ray scattering studies on proteins under extreme conditions," Ph.D. thesis (Technischen Universität Dortmund, 2011), Chap. 2.
22. S. Förster, N. Hermsdorf, W. Leube, H. Schnablegger, M. Regenbrecht, S. Akari, P. Lindner, and C. Böttcher, "Fusion of charged block copolymer micelles into toroid networks," J. Phys. Chem. B **103**, 6657–6668 (1999).
23. A. Mugnai and W. J. Wiscombe, "Scattering from nonspherical Chebyshev particles. I: cross sections, single-scattering albedo, asymmetry factor and backscattered fraction," Appl. Opt. **25**, 1235–1244 (1986).
24. H. Funaki, "Contributions on the shapes of red blood corpuscles," Jpn. J. Physiol. **5**, 81–92 (1955).
25. L. Bi and P. Yang, "Modeling of light scattering by biconcave and deformed red blood cells with the invariant imbedding T-matrix method," J. Biomed. Opt. **18**, 055001 (2013).
26. G. Valchev, V. M. Vassilev, and P. A. Djondjorov, "On different models describing the equilibrium shape of erythrocyte," Bulg. Chem. Commun. **42**, 84–94 (2015).
27. B. E. Treeby, "Acoustic attenuation compensation in photoacoustic tomography using time-variant filtering," J. Biomed. Opt. **18**, 036008 (2011).
28. B. E. Treeby and B. T. Cox, "k-wave: MATLAB toolbox for the simulation and reconstruction of photoacoustic wave fields," J. Biomed. Opt. **15**, 021314 (2010).
29. T. Rother, K. Schmidt, J. Wauer, V. Shcherbakov, and J. Gayet, "Light scattering on Chebyshev particles of higher order," Appl. Opt. **45**, 6030–6037 (2006).
30. M. Pharr and G. Humphreys, *Physically-Based Image Synthesis: From Theory to Implementation* (Elsevier, 2014), Chap. 14, pp. 497–520.